International Journal of Nanomedicine

Dovepress

open access to scientific and medical research

Open Access Full Text Article

ORIGINAL RESEARCH

Fluorescent Imaging-Guided Chemo- and Photodynamic Therapy of Hepatocellular Carcinoma with HCPT@NMOFs-RGD Nanocomposites

Yue Shang[1,*], Hui Zhang[2,*], Yajia Cheng[3], Peipei Cao[3], Jianlin Cui[3], Xuebo Yin[4], Saijun Fan[1], Yuhao Li[5]

[1]Institute of Radiation Medicine, Chinese Academy of Medical Sciences and Peking Union Medical College, Tianjin, People's Republic of China; [2]Shanghai Institute of Quality Inspection and Technical Research, Shanghai, People's Republic of China; [3]Department of Pathology, Nankai University School of Medicine, Tianjin, People's Republic of China; [4]College of Chemistry and Chemical Engineering, Shanghai University of Engineering Science, Shanghai, People's Republic of China; [5]Beijing Geriatric Medical Research Center, Xuanwu Hospital, Capital Medical University, Beijing, People's Republic of China

*These authors contributed equally to this work

Correspondence: Yuhao Li, Xuanwu Hospital, Capital Medical University, Beijing, 100053, People's Republic of China, Tel +86-10-83198269, Email liyuhao@xwh.ccmu.edu.cn

Background: Hepatocellular carcinoma (HCC), arising from hepatocytes, is the most common primary liver cancer. It is urgent to develop novel therapeutic approaches to improve the grim prognosis of advanced HCC. 10-hydroxycamptothecin (HCPT) has good antitumor activity in cells; however, its hydrophobicity limits its application in the chemotherapy of HCC. Recently, nanoscale porphyrin metal-organic frameworks have been used as drug carriers due to their low biotoxicity and photodynamic properties.

Methods: Nanoscale zirconium porphyrin metal-organic frameworks (NMOFs) were coated with arginine-glycine-aspartic acid (RGD) peptide to prepare NMOFs-RGD first. The HepG2 cell line, zebrafish embryos and larvae were used to test the biotoxicity and fluorescence imaging capability of NMOFs-RGD both in vitro and in vivo. Then, NMOFs were used as the skeleton, HCPT was assembled into the pores of NMOFs, while RGD peptide was wrapped around to synthesize a novel kind of nanocomposites, HCPT@NMOFs-RGD. The tissue distribution and chemo- and photodynamic therapeutic effects of HCPT@NMOFs-RGD were evaluated in a doxycycline-induced zebrafish HCC model and xenograft mouse model.

Results: NMOFs-RGD had low biotoxicity, good biocompatibility and excellent imaging capability. In HCC-bearing zebrafish, HCPT@NMOFs-RGD were specifically enriched in the tumor by binding specifically to integrin $\alpha_v\beta_3$ and led to a reduction in tumor volume. Moreover, the xenografts in mice were eliminated remarkably following HCPT@NMOFs-RGD treatment with laser irradiation, while little morphological change was found in other main organs.

Conclusion: The nanocomposites HCPT@NMOFs-RGD accomplish tumor targeting and play synergistic chemo- and photodynamic therapeutic effects on HCC, offering a novel imaging-guided drug delivery and theranostic platform.

Keywords: zirconium porphyrin metal-organic frameworks, 10-hydroxycamptothecin, hepatocellular carcinoma, chemotherapy, photodynamic therapy

Introduction

Hepatocellular carcinoma (HCC) is the most common primary liver cancer and has a high mortality rate due to its rapid progression, high malignancy and low cure rate.[1,2] Although early HCC can be managed by ablation,[3] the results of surgery are poor in patients with advanced disease due to the presence of extrahepatic infiltration and metastases.[4] Chemotherapy is one of the standard strategies for patients with advanced HCC.[5] Among

Received: 13 December 2021
Accepted: 10 March 2022
Published: 25 March 2022

chemotherapeutic drugs, 10-hydroxycamptothecin (HCPT), a topoisomerase I inhibitor, inhibits cell proliferation and has a broad spectrum of antitumor activity against breast, colon, lung, and ovarian cancers in clinical practice.[6,7] However, HCPT is insoluble in either water or acidic environments and can cause severe systemic side effects, limiting its administration in the treatment of HCC.[8] Therefore, modifying its hydrophobicity and reducing its adverse effects on normal organs will provide great help for its clinical application. In addition, multimodal therapy is the future trend of HCC treatment. Immunotherapy, molecular-targeted therapy, photodynamic therapy (PDT) and photothermal therapy (PTT) have been involved in the treatment of liver cancer.[9,10]

In recent years, a variety of nanomaterials have been used as carriers to deliver drugs to tumor tissues.[11–13] Among them, nanoscale porphyrin metal-organic frameworks, composed of metal ions and porphyrin organic ligands, stand out due to their tunable porosity, robust stability, fluorescent tracing and easy functionalization.[14,15] Low toxic metal ions, such as Fe^{2+}, Zn^{2+} and Zr^{4+}, provide the stability of the material, while porphyrin ligands are coupled by conjugated double bonds to form a reticulated skeleton.[16,17] Moreover, due to the electron-supplying substituents on its phenyl group, porphyrin can be used as a photosensitizer for imaging-guided localization, diagnosis or PDT.[18,19] Angiogenesis is a characteristic manifestation of tumor proliferation, which contributes greatly to tumor growth, infiltration and metastasis.[20] In tumor tissues, after degradation of the vascular basement membrane, vascular endothelial cells are activated, proliferated, migrated and reconstituted to form blood vessels and vascular networks.[21,22] Integrins are the primary extracellular matrix (ECM) receptors that provide a link between the external matrix scaffold and the internal actin cytoplasm.[23] Among integrins, integrin $\alpha_v\beta_3$ is highly expressed in both endothelial cells and pericytes and acts as a ligand on the cell membrane binding to the ECM containing an arginine-glycine-aspartic acid (RGD) motif.[24] Therefore, an RGD molecule-based drug delivery system enables targeted transport and release at the tumor site.

In this study, nanoscale zirconium-porphyrin metal-organic frameworks (NMOFs) were used as the carrier skeleton. HCPT was assembled into the pores of NMOFs, while RGD peptide was wrapped around NMOFs. Thus, a novel kind of nanocomposites, HCPT@NMOFs-RGD, were prepared. Subsequently, we determined the following properties of HCPT@NMOFs-RGD: 1) physical and chemical characterization; 2) in vitro and in vivo imaging capability and biotoxicity; 3) targeted delivery to tumor sites of HCC; and 4) chemo- and photodynamic-synergistic therapeutic effects on HCC. Our study combined fluorescence imaging-guided HCPT chemotherapy and PDT on HCC for the first time. This not only broadened the potential applications of engineered NMOFs by demonstrating their capability for precise targeted delivery but also provided a new approach to the treatment of HCC.

Materials and Methods

Cell Culture

The human HCC cell line HepG2 (purchased from ATCC) and human hepatocyte cell line L02 (purchased from Beijing Union Medical College Hospital) were cultured in complete Dulbecco's modified Eagle's medium (DMEM; Biological Industries (BI), Israel) and complete Roswell Park Memorial Institute 1640 (RPMI-1640) medium (BI), respectively, containing 10% (v/v) fetal bovine serum (BI) and 1% penicillin-streptomycin (Thermo Scientific, DE, USA). The use of cell lines was approved by the Institutional Ethics Committee at Nankai University. Both cell lines were incubated at 37 °C with 5% CO_2.

Experimental Animals

For fish experiments, wild-type zebrafish (AB strain) and transgenic zebrafish Tg (*fabp10:rtTA2s-M2; TRE2:EGFP-kras*^{G12V}) (*kras*^{G12V}; a gift from Dr. Gong) were raised under standard conditions with a 10-hour dark/14-hour light cycle at 28.5 °C.[25] For mouse experiments, 6- to 8-week-old male BALB/c mice (18–20 g, license No. SCXK-2014-003) were purchased from the Chinese Academy of Medical Sciences & Peking Union Medical College. All experimental protocols involving animals were approved by the Institutional Animal Care and Use Committee of Nankai University and complied with the Guide for the Care and Use of Laboratory Animals by the National Institutes of Health (NIH).

Reagents

The following reagents were used: zirconium chloride ($ZrCl_4$; Aladdin Chemistry Co. Ltd., Shanghai, China); polyetherimide (PEI, molecular weight =10,000; Fu Chen Reagent Co., Ltd., Tianjin, China); 5,10,15,20-tetrakis(4-carboxyl)-21H,23H-porphine (TCPP; TCI Chemical Ind. Develop Co., Shanghai. China); 9,10-anthracenediyl-bis (methylene) dimalonic acid (ABDA; Aladdin); 1-ethyl-3-(3-dimethylaminepropyl) carbodiimide (EDC; Aladdin); N-hydroxysuccinimide (NHS; Aladdin); 10-hydroxycamptothecin (HCPT; Sigma-Aldrich, St. Louis, MO, USA); arginine-glycine-aspartic acid tripeptide (RGD; Peptide Co., Ltd., Shanghai, China); and dimethylformamide (DMF; Concord Reagent Co., Tianjin, China). All reagents were of at least analytical grade and were used as purchased without further purification.

Preparation of NMOFs-RGD and HCPT@NMOFs-RGD

$ZrCl_4$ (5 mg), TCPP (0.009 $mmoL^{-1}$) and 0.5 mL acetic acid in 16 mL of DMF were ultrasonically dissolved in a 20 mL Pyrex vial. The mixture was heated in a 120 °C oven for 12 h to obtain NMOFs. NMOFs were then dissolved in 10 mL DMF, and 5 mg PEI was added while stirring for 2 h at room temperature. The mixture was centrifuged and dispersed in 10 mL distilled water. EDC (5 mg) and NHS (5 mg) were added and stirred for 12 h. The unreacted EDC and NHS were removed by centrifugation. Finally, 2 mg RGD was added to the solution for further reaction for 24 h, and NMOFs-RGD was obtained by centrifugation. For the preparation of HCPT@NMOFs-RGD, the above mixture was centrifuged and dispersed in 10 mL DMF containing 20 mg HCPT for 24 h. The resulting HCPT@NMOFs were dispersed in 10 mL distilled water. The remaining steps were the same as the preparation of NMOFs-RGD.

Instrumentation and Characterization

The instrumentation used in the analytical experiments was as follows: transmission electron microscopy (TEM) images were recorded with a Tecnai G2 F20 (FEI, Hillsboro, OR, USA; accelerating voltage=200 kV). X-ray diffraction (XRD) patterns were obtained by a D/max-2500 diffractometer (Rigaku, Tokyo, Japan) using Cu-Kα radiation (λ=1.5418 Å). The Zr content was measured by inductively coupled plasma atomic emission spectroscopy (ICP-AES; IRIS advantage, Thermo, USA). N_2 adsorption-desorption isotherms and the pore size distribution were tested by TriStar 3000 (Micromeritics, Norcross, GA, USA) at 77 K. The pore-size distribution was calculated by the Barrett, Joyner and Halenda (BJH) method according to the density functional theory (DFT) program. UV-Vis absorption spectra were recorded by a UV-2450-visible spectrophotometer (Shimadzu, Japan). The steady-state fluorescence experiments were performed on an FL-4600 Fluorescence Spectrometer (Hitachi, Japan) equipped with a plotter unit and a quartz cell (1 cm × 1 cm). The slit width was 5 nm for both excitation (560 nm) and emission. Infrared spectra were obtained by Bruker TENSOR 27 Fourier transform infrared spectroscopy. Thermogravimetric analysis (TGA) was performed on a PTC-10ATG-DTA analyzer heated from 20 °C at a ramp rate of 10 °C min^{-1} under air. The singlet oxygen ($^1O_2$) generation of NMOFs upon laser irradiation was conducted using the ABDA method. A mixed solution of NMOFs-RGD (20 mM) and 200 mM ABDA was irradiated with a 655 nm laser (light intensity 1000 mW cm^{-2}). At each predetermined time interval, the absorbance spectra were recorded. The drug release experiment of HCPT@NMOFs-RGD was carried out by the dynamic dialysis method. 10 mg HCPT@NMOFs-RGD was dispersed in 3 mL PBS (0.01 M, pH 7.4) and sealed in a dialysis bag (MWCO 4000 Da), which was immersed in 50 mL PBS. Within the specified time period, 100 μL of media was collected to detect the HCPT content. The amount of released HCPT in the solution was measured with an FL fluorescence spectrometer at λ_{ex}=319 nm and λ_{em}=650 nm.

In vitro Cytotoxicity Assay

HepG2 cells were seeded in a 96-well plate (1×10^4 cells/well) and incubated with 100 μL of culture medium containing NMOFs (0, 25, 50, 100, 200, and 400 μg/mL), NMOFs-RGD (0, 25, 50, 100, 200, and 400 μg/mL), or HCPT@NMOFs-RGD (0, 25, 50, 100, 200, and 400 μg/mL) for 6 h. In vitro cytotoxicity was determined using the MTT assay according to the manufacturer's instructions (Keygen Biotech, Jiangsu, China). For the PDT test, cells incubated with NMOFs-

RGD or HCPT@NMOFs-RGD were irradiated with a laser at 655 nm for 10 min (300 mW cm^{-2}) before the MTT assay. For each sample, three parallel replicates were measured.

In vitro Biological Imaging

HepG2 cells were seeded in a 24-well plate (4×10^4 cells/well) in 500 μL of medium and cultured overnight. Cells were then incubated with fresh DMEM containing RGD-labeled NMOFs at concentrations of 0 (control), 25, 50, 100, 200, and 400 μg/mL for 6 h, washed with PBS (0.01 M, pH 7.4) three times, fixed with 4% paraformaldehyde (PFA) and labeled with 4.6-diamino-2-phenylindole (DAPI; diluted at 1:1000; Sigma–Aldrich) for 10 minutes. Three parallel replicates were measured at each concentration. Fluorescence images were photographed with an FV 1000 confocal microscope (Olympus Corporation, Tokyo, Japan). Red fluorescence images of NMOFs-RGD were captured using 559 nm excitation; blue fluorescence of the DAPI staining was acquired using 405 nm excitation.

In vitro Singlet Oxygen Generation Detection

Singlet oxygen ($^1O_2$) generation was detected using a 2′,7′-dichlorofluorescin diacetate (DCFH-DA) probe.[26] HepG2 cells were seeded in a 24-well plate (4×10^4 cells/well) and cultured for 24 h. Cells were then incubated with NMOFs-RGD or HCPT@NMOFs-RGD at a concentration of 200 μg/mL for 6 h. After removing the residual NMOFs-RGD or HCPT@NMOFs-RGD, DCFH-DA (10 μM in PBS) was added to the cells and incubated for 1 h. The cells were washed three times with PBS and irradiated with a laser at 655 nm for 10 min (300 mW cm^{-2}). The generated $^1O_2$ was captured under an FV 1000 confocal microscope (Olympus) with an excitation wavelength of 488 nm and emission wavelength of 520 nm.

Aqueous Exposure on Zebrafish Embryos and Larvae

To evaluate the in vivo biological imaging, wild-type zebrafish embryos were collected at 1 hour postfertilization (hpf), placed in a 24-well plate (50 embryos/well), and exposed continuously to NMOFs-RGD at concentrations of 25, 50, 100, and 200 μg/mL. Embryos incubated in sterilized 1 × Holt buffer (3.5 g/L NaCl, 0.05 g/L KCl, 0.025 g/L $NaHCO_3$, 0.1/L $CaCl_2$, pH 7.2) were used as the control. Each well contained 3 mL NMOFs-RGD solution or Holt buffer. After 5 hours, embryos were rinsed with Holt buffer (5 minutes each, three times) and observed under a BX51 fluorescence microscope (Olympus). To observe the distribution of NMOFs-RGD in larvae, wild-type fish at 5 days postfertilization (dpf) were exposed to NMOFs-RGD at a concentration of 200 μg/mL for 12 hours. Bright-field and fluorescent images were captured every 12 h until the fluorescence disappeared.

Induction and Chemotherapy of HCC in Zebrafish

To induce HCC in zebrafish, 1-month-old *kras*^{G12V} juveniles were treated with doxycycline (D9891; Sigma-Aldrich) at a concentration of 60 μg/mL for 15 days in the dark as described previously.[27] HCC-bearing fish were treated with HCPT@NMOFs-RGD at a concentration of 200 μg mL^{-1} for 4 days.

Fluorescence-Guided Chemotherapy and PDT on Xenograft Tumor

For the tumor xenograft experiment, 3×10^6 HepG2 cells were suspended in PBS (0.01 M, pH 7.4) and injected subcutaneously into the thigh flank region of BALB/c nude mice. The tumor volumes of the mice were measured as ($width^2$ × length)/2. When the volume was approximately 80 mm^3 (~ 2 weeks after injection), the tumor-bearing mice were divided randomly into four groups (n = 4 in each group): chemotherapy, PDT, synergetic therapy, and control groups. In the chemotherapy group, mice were injected with HCPT@NMOFs-RGD (200 μL, 1 mg mL^{-1}) through the caudal vein. In the PDT group, mice were injected with NMOFs-RGD (200 μL, 1 mg mL^{-1}) and irradiated with a 655 nm laser (1000 mW·cm^{-2}) for 30 min after 24 hours. In the synergetic group, mice were injected with HCPT@NMOFs-RGD (200 μL, 1 mg mL^{-1}) and irradiated with a 655 nm laser (1000 mW·cm^{-2}) for 30 min after 24 hours. PBS-injected mice were used as the control. The administration for all the mice from the four groups was repeated every 4 days. The tumor volume was measured every 2 days until 12 days postinjection.

Thermal Imaging

Thermal imaging was performed with a NightOWL LB 983 small animal in vivo imaging system (Berthold Technologies GmbH & Co. KG, Germany) under the condition of the emission wavelength of HCPT@NMOFs-RGD (Ex=530 nm, Em=660 nm). HCC-bearing fish were anaesthetized in 0.016% tricaine (A5040; Sigma-Aldrich), euthanized immediately, collected and thermally imaged at 24, 48, 72 and 96 hours post treatment (hpt). In mice, thermal imaging was then performed in NMOFs-RGD-injected tumor-bearing mice at 0, 1, 6, 12 and 24 hours postinjection.

Hematoxylin and Eosin (HE) and Immunofluorescence Staining

Hematoxylin and eosin (HE) staining and immunofluorescence were performed using standard protocols.[28] HCC-bearing fish were anaesthetized in 0.016% tricaine and euthanized immediately. The livers were dissected and fixed in 4% PFA overnight at 4 °C. For cell immunofluorescence staining, L02 or HepG2 cells were seeded in a 24-well plate at a density of 4×10^4 in 500 μL/well and grown on glass coverslips. The primary antibody was anti-integrin $\alpha_v\beta_3$ antibody (1:500; ab7166, Abcam, Cambridge, MA, USA). The secondary antibody was a fluorescently labeled Cy3 (1:200; Millipore, Billerica, MA, USA). The sections were counterstained with DAPI (1:1000, Sigma) to label the nuclei.

Statistical Analysis

Quantitative data were analyzed using GraphPad Prism software (version 8.0, GraphPad Software Inc., San Diego, CA, USA). For image analysis, ImageJ software (1.49X, NIH, http://rsb.info.nih.gov/ij/) was used to convert images to 8-bit greyscale prior to thresholding, subsequently calculated the area of positive signals, the area of nuclei, or the intensity of fluorescence. The fluorescence intensity, viability of cells and tumor weight are shown as percentages (means ± SEM). Values between two groups were compared with Student's *t*-test. Data among three or more groups were analyzed using one-way analysis of variance (ANOVA). $P<0.05$ were considered statistically significant.

Results and Discussion

Schematic Illustration and Characterization of HCPT@NMOFs-RGD

Nanoscale porphyrin metal-organic frameworks are a class of porous materials. They circumvent the hydrophobic nature, meanwhile, their ultra-large channels can carry polycyclic molecules or drugs. The photophysical properties of porphyrin offers an approach to monitor and track the nanocomposites.[29] In the present study, we designed and synthesized a novel zirconium-porphyrin metal-organic frameworks-based nanocomposite, HCPT@NMOFs-RGD, and investigated the targeted administration to HCC. A schematic illustration of HCPT@NMOFs-RGD is shown in Figure 1A. The structure and function of NMOFs were determined by the selection of metal ions and the regulation of organic ligands.[30] In our design strategy, Zr^{4+} was selected as the metal ion due to its low toxicity and promising biocompatible characteristics.[31] TCPP was used as the organic ligand to exhibit powerful fluorescence and served as a photosensitizer.[32] The combination of Zr^{4+} and TCPP formed a spherical skeleton with mesh-like pores to provide space for drug loading. HCPT, an anticancer drug, was assembled into the pores of NMOFs. The NMOFs were then functionalized with the ligand c-RGD coated on the surface of HCPT@NMOFs to give them targeting ability. The TEM images showed that NMOFs were in a monodisperse state and had a spherical structure with a particle size of approximately 90 nm in diameter (Figure 1B). Dynamic light scattering (DLS) analysis showed that NMOFs had a relatively narrow size distribution (d=136.8 nm; Figure S1A). Nitrogen adsorption indicated that the Brunauer-Emmett-Teller (BET) surface area of the NMOFs was ~1900 m^2/g and that its pore volume was ~0.67 cm^3/g (Figure S1B). In addition, it was observed that the size of the DFT pores was 1.25 nm, which was consistent with the results from the theoretical prediction (Figure 1C). The precisely matched peaks in small angle sections by powder X-ray diffraction (PXRD) patterns confirmed that the crystal structure of NMOFs was maintained (Figure S1C). Figure S1D showed the UV-vis absorption spectra of the TCPP ligand and NMOFs. The NMOFs had a similar pattern to the TCPP ligand, where the Soret band had a redshift at 420 nm and the Q bands had some redshifts at 525, 561, 590, and 650 nm. The redshift was attributable to the increase in the conjugation area of porphyrin after the NMOFs were formed. The 15 nm RGD layer was clearly observed around the NMOFs, as shown in the TEM image (Figure 1D). Both thermal gravimetric analysis (TGA) and Fourier transform infrared (FTIR) spectra confirmed the bioconjugation of RGD peptide on the NMOFs (Figure S1E and S1F). The NMOFs-

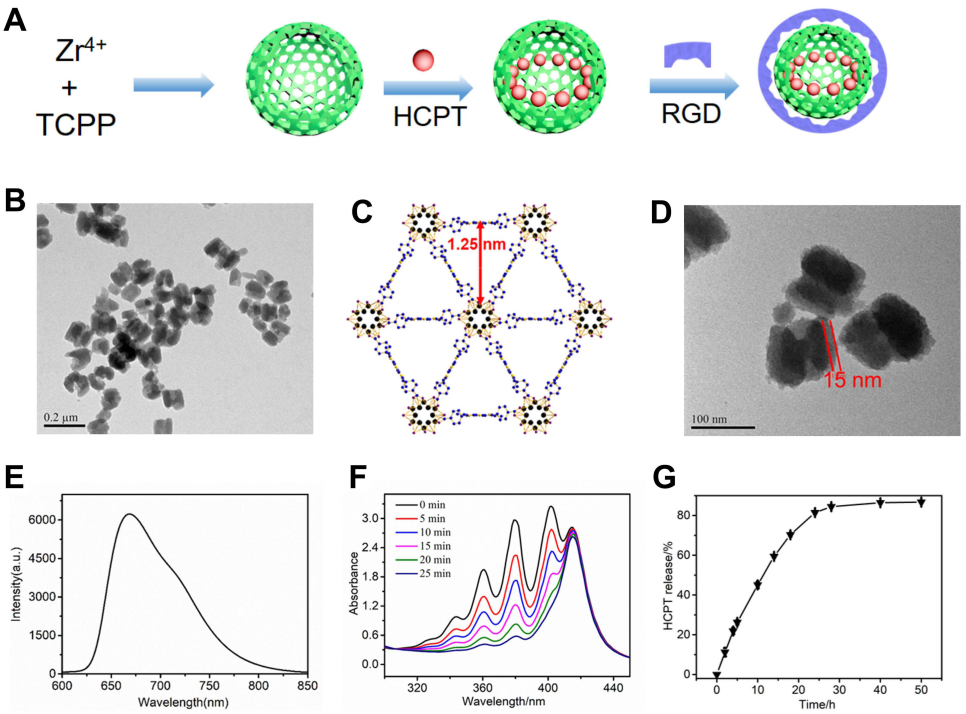

Figure 1 Synthesis and characterization of HCPT@NMOFs-RGD. (**A**) Scheme for the synthesis of HCPT@NMOFs-RGD nanocomposites. (**B**) TEM image of NMOFs. (**C**) View of NMOFs with uniform triangular 1D channels observed in the structure. (**D**) TEM images of NMOFs-RGD. Note that the RGD layer is distributed around the NMOFs at a thickness of 15 nm. (**E**) Fluorescence spectra (excitation at 530 nm) of NMOFs-RGD aqueous solution. (**F**) Absorbance spectra of ABDA in the presence of NMOFs-RGD over different periods under laser irradiation at 655 nm. (**G**) HCPT release performance of HCPT@NMOFs-RGD nanocomposites in PBS. Scale bar in (**B**): 0.2 μm; (**D**): 100 nm.

RGD had a strong emission wavelength at 660 nm when excited at 530 nm (Figure 1E). ABDA was used to test the PDT ability of NMOFs-RGD. Due to the high penetration depth, 655 nm laser irradiation was selected for $^1O_2$ generation. The produced $^1O_2$ oxidized ABDA, which was monitored as the decreased ABDA absorption at 379 nm (Figure 1F). The loading efficiency of HCPT was 88% (w/w), which was attributed to the electrostatic and noncovalent interactions between HCPT and the NMOFs. The fast release of HCPT was observed (50% after 12 h and 80% after 24 h) in a mimic biological environment (Figure 1G).

Imaging Ability and Biotoxicity of NMOFs-RGD

The toxicity of nanomaterials is a prerequisite for evaluating their applications. The in vitro imaging ability and toxicity of the NMOFs-RGD were tested in HepG2 cells.[33] Following 6 hours of incubation, red fluorescent signals were detected at the membrane and in the cytoplasm (Figure 2A). To quantify this finding, we scored the ratio between the area of NMOFs-RGD-positive signals and the area of nuclei. The results showed that the imaging of NMOFs-RGD was dose-dependent (Figure 2B; Student's *t*-test, $*P<0.05$, $**P<0.01$). The MTT assay results showed that the cell viability of the NMOFs-RGD group was higher than 85%, even at a concentration of 400 μg mL^{-1}. No significant difference was found between the NMOFs and NMOFs-RGD groups at each concentration (Figure 2C; ANOVA, $P>0.05$), indicating a low cytotoxicity of NMOFs-RGD. The in vivo toxicity and imaging ability of NMOFs-RGD was observed in zebrafish embryos and larvae. Zebrafish are considered as an ideal model for evaluating in vivo toxicity due to the characteristics of large amounts of spawning, transparent embryos and rapid development.[34] The pores on the surface of the chorion were approximately 600 nm in diameter.[35] NMOFs-RGD, with a size of ~90 nm in diameter, can enter the embryo through the pores. Following 5 hours of exposure to NMOFs-RGD, red fluorescent signals were mainly in the yolk and intensified in a dose-dependent manner (Figure S2). We also observed the phenotype of zebrafish embryos. Compared to the control group, no obvious malformation, such as pericardial edema and axial curvature, was found in the gross development in any NMOFs-RGD-exposed group until 72 hpf (Figure S3). Zebrafish larvae at 5 dpf were exposed to

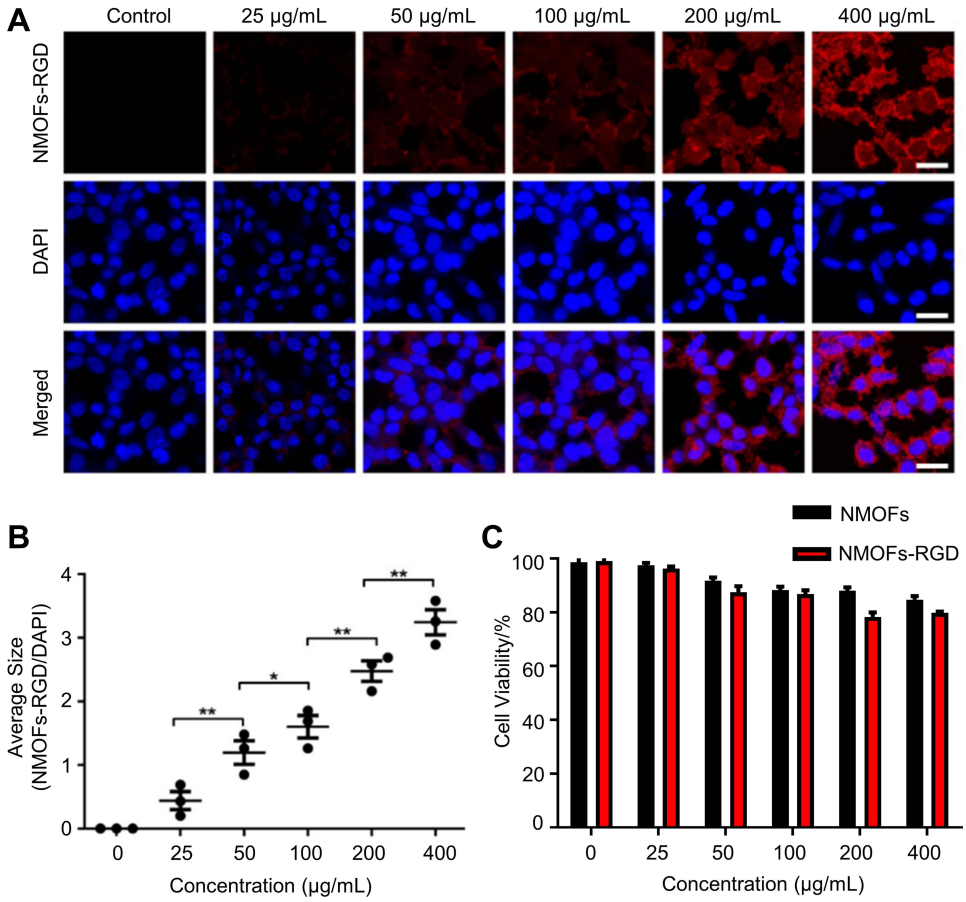

Figure 2 In vitro fluorescence imaging and cytotoxicity of NMOFs-RGD. (**A**) Fluorescence images of HepG2 cells exposed to NMOFs-RGD. Red signals are from NMOFs-RGD. Note that NMOFs-RGD are localized at the membrane and in the cytoplasm. (**B**) Statistical analysis of fluorescence intensity in NMOFs-RGD-incubated cells (Student's *t*-test; **P*<0.05, ***P*<0.01). (**C**) Statistical analysis of cell viability in HepG2 cells incubated with NMOFs (control) and NMOFs-RGD. Scale bar in (**A**): 20 μm.

NMOFs-RGD for 12 hours to determine the absorption, distribution, metabolism, and excreted (ADME) process of NMOFs-RGD. At 5 dpf, larvae can swim and prey, most organs have been well developed, and the gastrointestinal tract has already played its preliminary function.[36,37] The fluorescent signals were recorded until 72 hours post exposure (hpe). At 12 hpe, bright red signals accumulated mainly in the stomach and proximal intestine. Then, the positive signals moved to the distal intestine gradually, weakened along the exposure time and disappeared almost at 72 hpe (Figure 3A–C). This suggested that NMOFs-RGD entered the larvae and were excreted from the gastrointestinal tract with a retention time of approximately 60 hours. Taken together, the above data demonstrate that NMOFs-RGD have low biotoxicity and excellent bioimaging ability, both in vitro and in vivo, making NMOFs-RGD an ideal carrier for further modification and drug loading.

Targeting Delivery of NMOFs-RGD to HCC by Binding to Integrin $\alpha_v\beta_3$

In this study, the targeting efficiency was achieved by both passive and active methods. It is well known that nanocomposites can accumulate in tumor sites due to the passive targeting effect, named the enhanced permeability and retention (EPR) effect.[38–40] However, the EPR effect is short, and the heterogeneity of tumor tissue may impede drug delivery.[41] Identifying molecular markers of tumor tissue is a common strategy for active delivery. Integrin $\alpha_v\beta_3$ is widely expressed in neovascularization-rich tissues and can selectively bind to RGD.[42,43] RGD is a tumor homing peptide with cell penetration properties. RGD binds to the neuromucin-1 receptor to initiate protease hydrolysis and promote endocytosis.[44] Thus, the RGD-coated nanocomposites enable the molecular probe RGD to target the tumor cells actively and penetrate the membrane of tumor cell. Based on this, we coated RGD molecules with NMOFs to exert an active

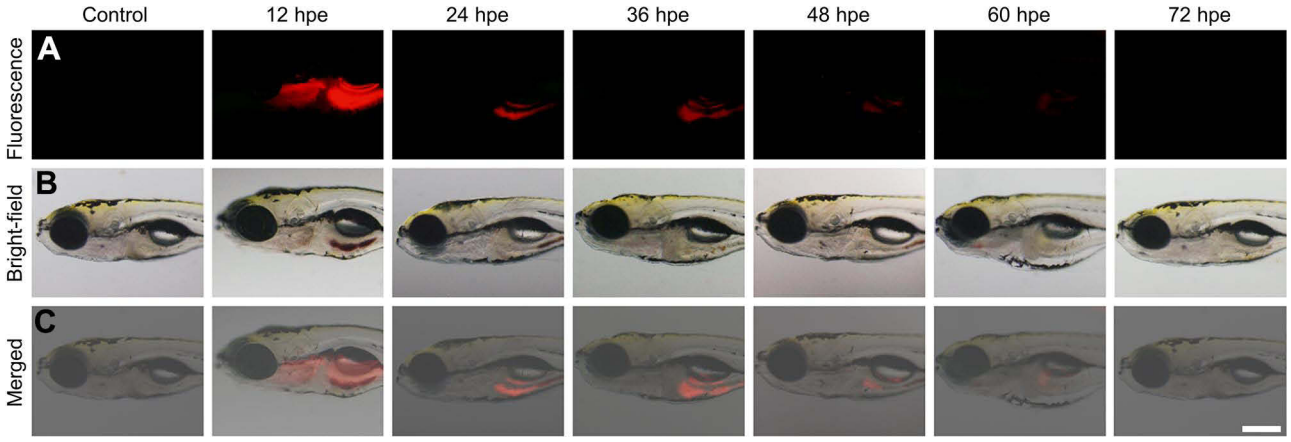

Figure 3 Time-lapse distribution of NMOFs-RGD in zebrafish larvae. (**A**) Fluorescence and (**B**) bright field images of NMOFs-RGD-exposed larvae at different hours post exposure (hpe). Red fluorescence was emitted by NMOFs-RGD. (**C**) Merged images from (**A** and **B**). Scale bar: 100 μm.

targeting effect. The targeting property of NMOFs-RGD was verified by three aspects. Firstly, at cell level, we detected whether integrin $\alpha_v\beta_3$ was only expressed in tumor cells. No positive signal was found in normal hepatocyte L02 cells (Figure S4A). However, integrin $\alpha_v\beta_3$ was strongly expressed in HepG2 cells and located at the membrane and in the cytoplasm (Figure S4B). Secondly, we tested the targeting ability with doxycycline-induced *kras*^{G12V} zebrafish HCC model. With induction time, the liver was enlarged with gradually strengthened green fluorescent signals (Figure S5A and S5B). Following 15 days of induction, the liver lost its normal morphology. The hepatic cords were disorganized, and the cells showed remarkable pleomorphism with a higher ratio of nucleus to cytoplasm (Figure S5C), indicating that homogeneous HCC was developed with the similar morphology and biology to human HCC.[45] In HCC-bearing zebrafish, integrin $\alpha_v\beta_3$-positive signals were densely distributed in tumor tissues (Figure 4A). Following NMOFs-RGD exposure, numerous red fluorescent signals were detected in the liver. They were circular and distributed around the nuclei, which was consistent with the expression pattern of integrin $\alpha_v\beta_3$ (Figure 4B). The co-localization of integrin $\alpha_v\beta_3$ and NMOFs-RGD suggested that NMOFs-RGD were targeted delivered to tumor tissue by recognizing integrin $\alpha_v\beta_3$, laying the foundation for the chemo- and photodynamic therapy. Finally, we verified the targeting ability with mice model. NMOFs-RGD were injected, and small animal imaging was used to track the tissue distribution in the following 24 hours. In both control and tumor-bearing mice, weak signals were detected throughout the body after 1 hour, and the

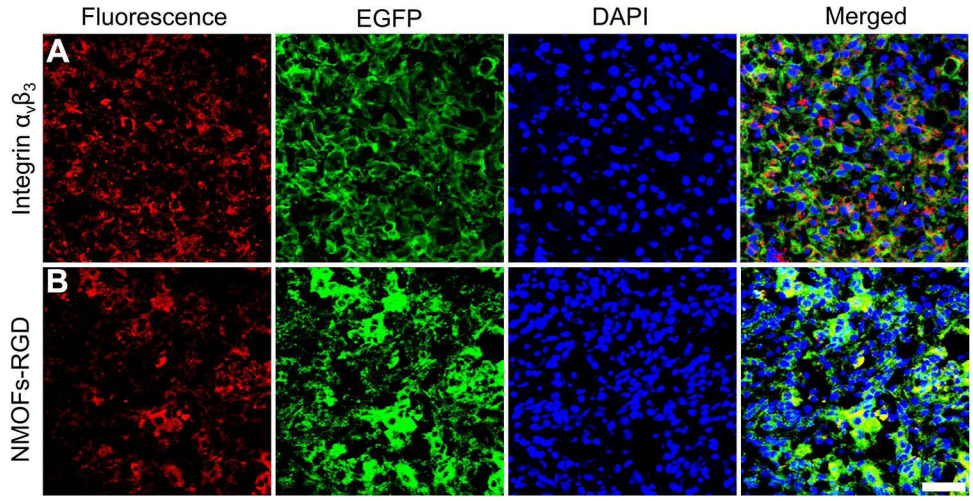

Figure 4 Targeted delivery of NMOFs-RGD to tumor tissue in HCC-bearing zebrafish. (**A**) The expression of integrin $\alpha_v\beta_3$. Red fluorescent signals are from integrin $\alpha_v\beta_3$-expressing cells. (**B**) The distribution of NMOFs-RGD in the liver of HCC *kras*^{G12V} zebrafish. Red fluorescent signals are from NMOFs-RGD. Scale bar: 20 μm.

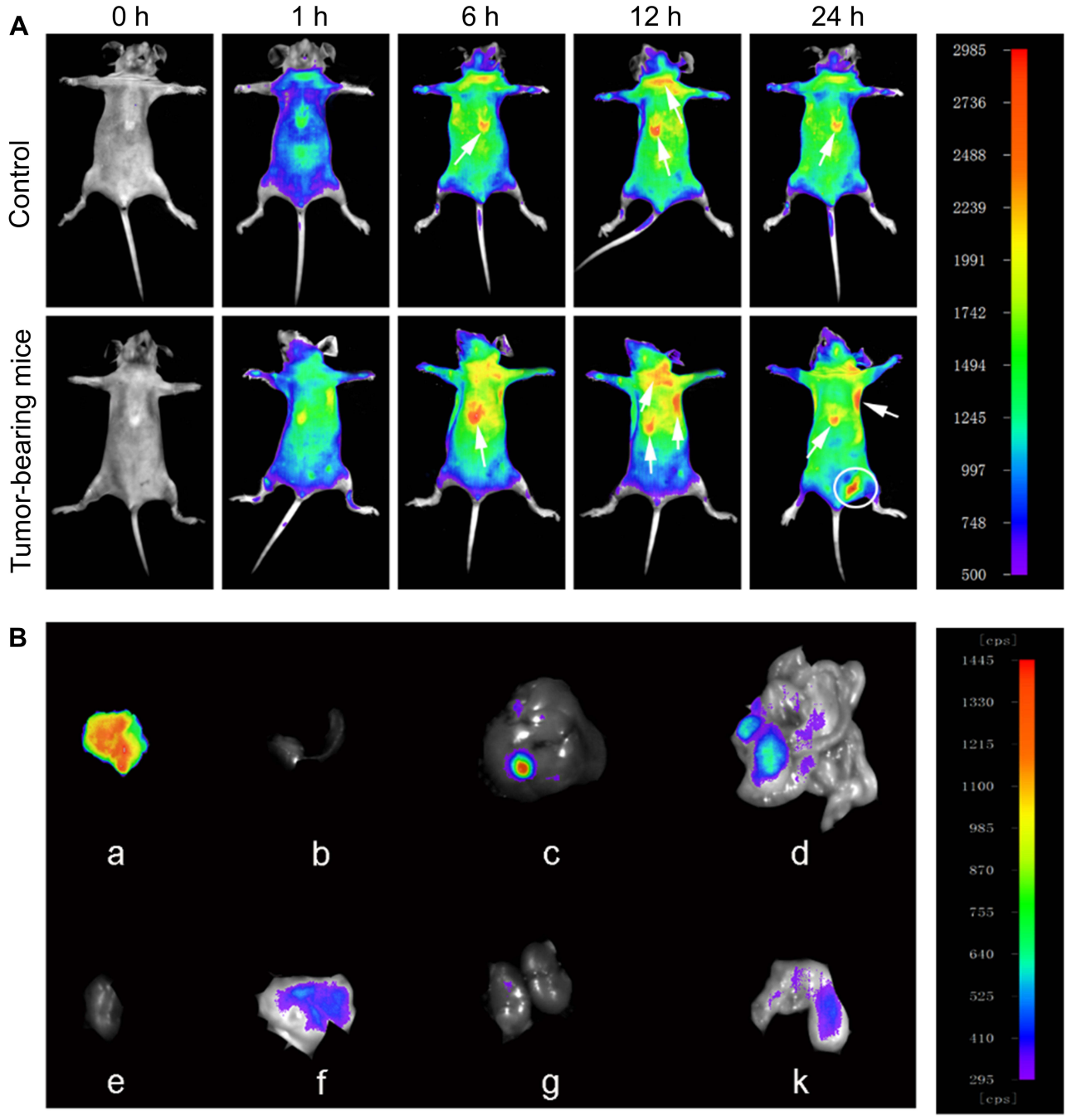

Figure 5 Time-lapse distribution of NMOFs-RGD in tumor-bearing mice. (**A**) Thermal images of NMOFs-RGD in control and tumor-bearing mice at 0, 1, 6, 12, and 24 hours (h) postinjection. (**B**) Thermal images of NMOFs-RGD in different organs of tumor-bearing mice: (a) tumor, (b) spleen, (c) liver, (d) intestine, (e) heart, (f) stomach, (g) kidney, and (k) lung.

intensity of the signals increased along the injection time, mainly located at the thymus gland and lymph nodes (arrows; Figure 5A). Surprisingly, at 24 hours post injection, a strong signal area was detected at the xenograft tumor site (circle; Figure 5A). We dissected the mice and tested the intensity of thermal imaging from different organs. No or very weak signals were shown in the heart, spleen, or kidneys. Signals of moderate intensity were detected in the liver and intestine. In contrast, signals from tumor sites were very strong (Figure 5B). This indicates that NMOFs-RGD are enriched in liver tumor sites, due to the accurate identification of RGD with integrin $\alpha_v\beta_3$. It was reported that epidermal growth factor receptor (EGFR) was overexpressed in HCC and played an important role in the tumor microenvironment.[46] Also, EGFR

regulated the activation of integrin $\alpha_v\beta_3$ and can increase tumor cell growth, proliferation, and metastasis mediated by cell adhesion.[47] Further test of EGFR in this HCC model should yield results for better understanding the targeting delivery of NMOFs-RGD.

Chemotherapy and Synergetic Therapy of HCPT@NMOFs-RGD on HCC

For HCC treatment, we demonstrated the chemotherapy in zebrafish first. HCC-bearing *kras*^{G12V} fish were continuously treated with HCPT@NMOFs-RGD for 4 days. HCPT@NMOFs-RGD entered the fish by swallowing and/or skin penetration.[48] The chemotherapeutic effect was evaluated by thermal imaging, gross appearance and EGFP fluorescence every 24 hours post treatment (Figure 6A–C). The fish abdomen became brighter from 24 to 48 hpt and darkened gradually at 72 and 96 hpt (Figure 6A). At each time point, fish were euthanized and photographed to show the gross appearance (Figure 6B). Then, the livers were dissected to observe the fluorescence. EGFP-positive signals were strong and bulky before HCPT@NMOFs-RGD treatment, diminished gradually over the treatment time, and weakened at 96 hpt (Figure 6C). Statistical analysis showed that the intensity of thermal imaging signals reached its peak at 48 hpt and

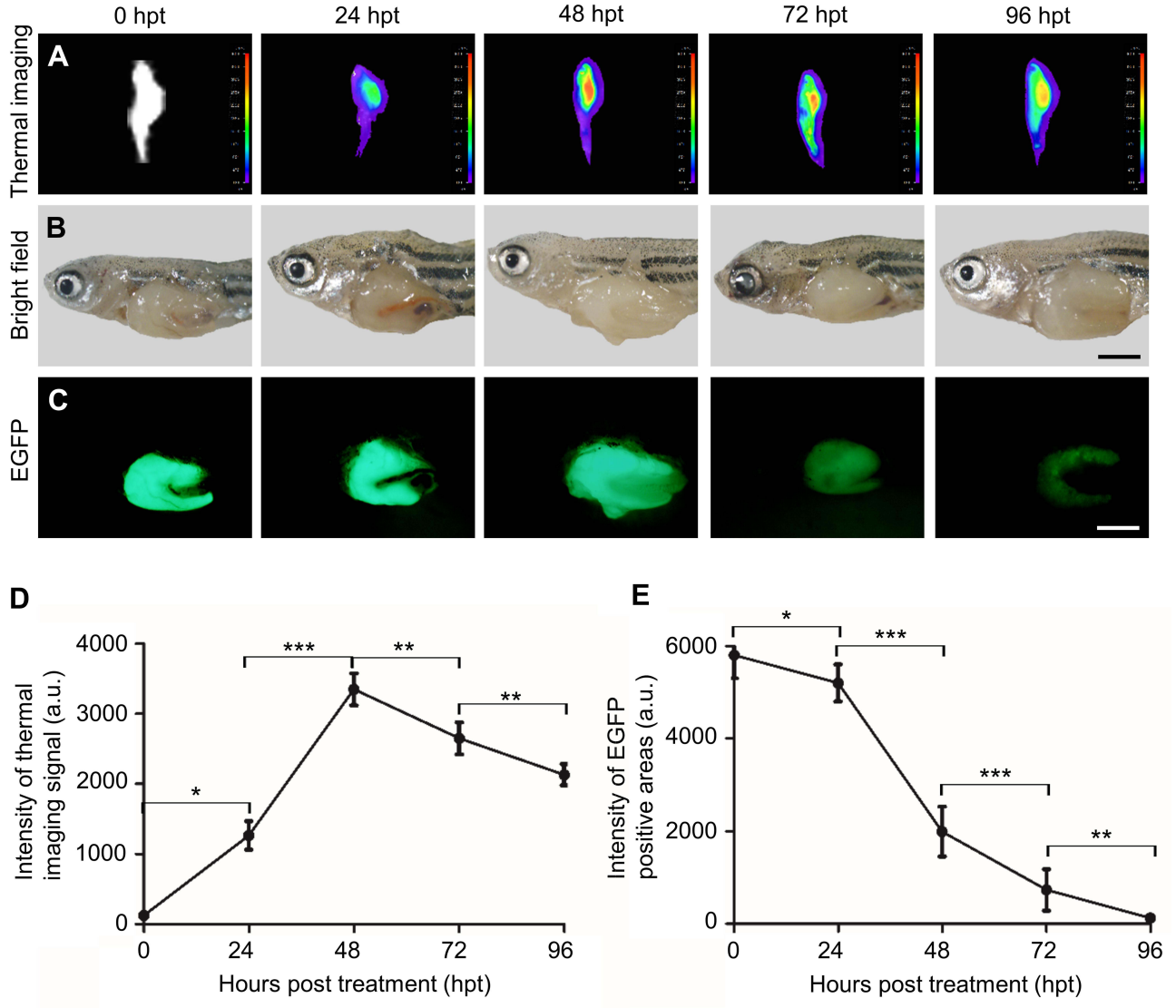

Figure 6 The chemotherapeutic effect of HCPT@NMOFs-RGD in HCC-bearing zebrafish. (**A**) Thermal imaging, (**B**) bright field, and (**C**) EGFP fluorescence of HCC-bearing zebrafish following HCPT@NMOFs-RGD treatment at 0 (control), 24, 48, 72, and 96 hours post treatment (hpt). (**D**) Statistical analysis of the intensity of thermal imaging (n=3 at each time point; ANOVA, **P*<0.05, ***P*<0.01, ****P*<0.001). (**E**) Statistical analysis of the intensity of EGFP-positive areas (n=3 at each time point; ANOVA, **P*<0.05, ***P*<0.01, ****P*<0.001). Scale bar in (**B** and **C**): 200 μm.

declined at 72 and 96 hpt (Figure 6D; ANOVA, *P<0.05, **P<0.01, ***P<0.001). Moreover, the intensity of EGFP fluorescence diminished dramatically at 24, 48, 72 and 96 hpt (Figure 6E; ANOVA, *P<0.05, **P<0.01, ***P<0.001). We then performed cryosectioning and DAPI staining on the dissected livers to verify the morphology. The red fluorescent signals emitted from HCPT@NMOFs-RGD emerged at 24 hpt, became brightest at 48 hpt and gradually decreased at 72 and 96 hpt, which was consistent with the thermal imaging results (Figure 7A). In contrast, EGFP fluorescence decreased with treatment time and was very faint at 96 hpt (Figure 7B). HCPT@NMOFs-RGD was distributed on the cell membrane and partially colocalized with EGFP-positive signals (Figure 7C and D). The prepared HCPT@NMOFs-RGD solved the hydrophobicity of HCPT and can be used as imaging-guided therapy systems (IGTSs). During 4-day administration, HCPT were not only enriched specifically in the tumor site, but also released continuously from the nanocomposites and played chemotherapeutic effects, leading to the dramatic reduction on tumor tissues in an HCC-bearing zebrafish model.

In order to maximize tumor suppression while minimizing toxicity to other organs, there is a trend to develop multimodal therapy.[49] PDT is a therapeutic approach involving light and photosensitizer. In HCPT@NMOFs-RGD, porphyrin was used for fluorescence imaging as well as acted as a photosensitizer.[50] After exposure to light at a specific wavelength, the porphyrin was activated to generate singlet oxygen and exert a toxic effect on tumor cells rather than damaging the neighboring tissue.[51] Based on this, we examined the ability of $^1O_2$ generation in NMOFs-RGD and

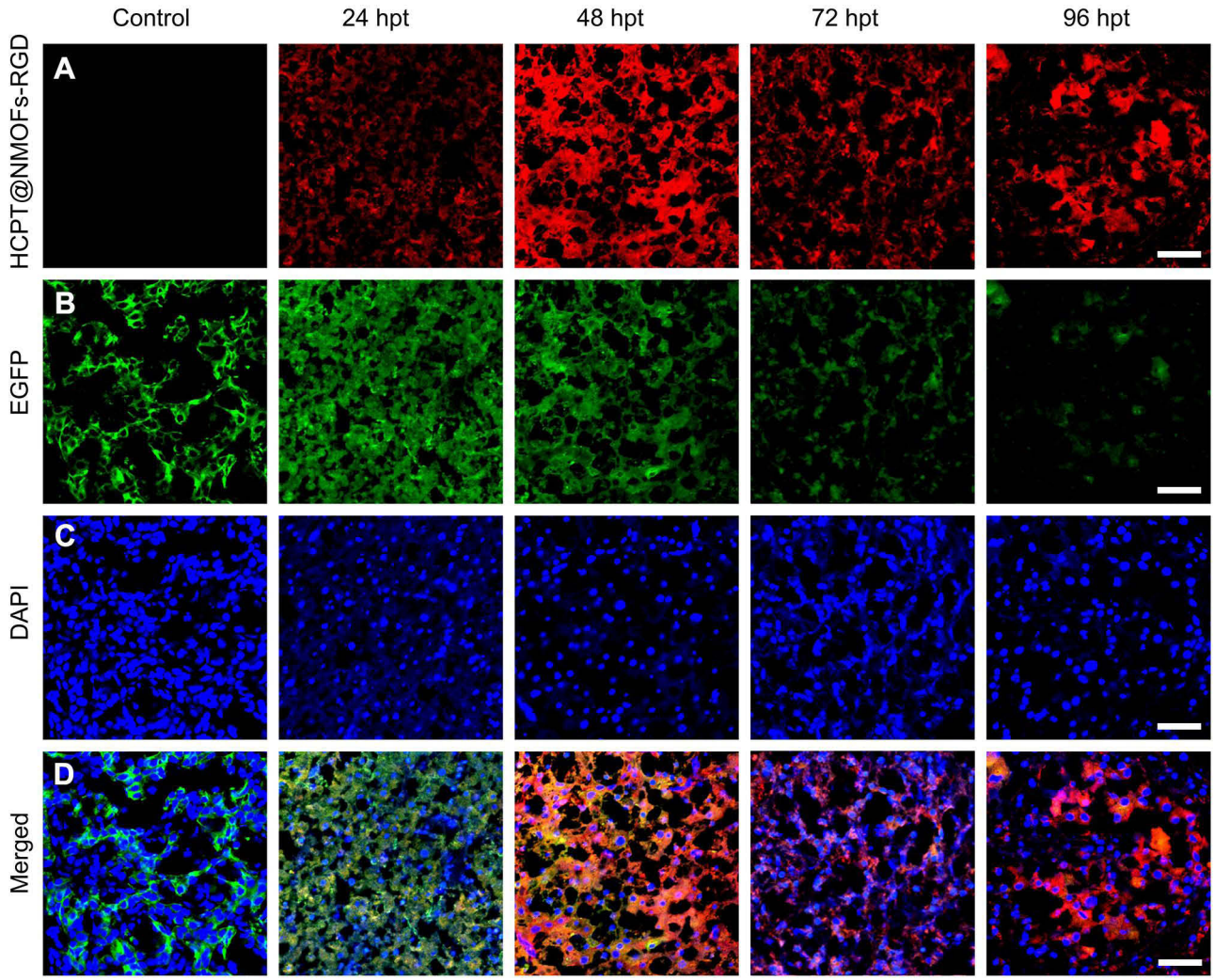

Figure 7 Time-lapse appearance of livers in HCC-bearing zebrafish following HCPT@NMOFs-RGD treatment. (**A**) Images of HCPT@NMOFs-RGD distribution in livers at 0 (control), 24, 48, 72, and 96 hours post treatment (hpt). (**B**) Images of EGFP fluorescence. (**C**) DAPI staining. (**D**) Merged images of (**A**–**C**). Scale bar: 20 μm.

HCPT@NMOFs-RGD with HepG2 cells. The DCFH-DA probe can bind to $^1O_2$ and emit green fluorescent signals.[52,53] Following laser irradiation, HepG2 cells from the NMOFs-RGD- or HCPT@NMOFs-RGD-incubated groups showed strong green fluorescence signals, while only weak green fluorescence signals were detected in the no-light group (Figure S6A). The MTT assay showed that the cell survival rates were significantly decreased following laser irradiation, indicating effective cell killing. Moreover, the higher the concentration of NMOFs-RGD or HCPT@NMOFs-RGD was, the higher the killing efficiency (Figure S6B and S6C; ANOVA, *P<0.05, **P<0.01). These data demonstrate that NMOFs-RGD and HCPT@NMOFs-RGD can kill tumor cells by photodynamic effects. Our design strategy on HCC therapy was that HCPT@NMOFs-RGD can exert the photodynamic therapeutic effect while the release of HCPT plays chemo-therapeutic role. Therefore, we investigated the in vivo synergetic therapy of HCPT@NMOFs-RGD on xenografts of mice. After 12 days of treatment, the tumor sizes from both the PDT and chemotherapy groups were smaller than that of the control group (Figure 8A). Surprisingly, tumors in the synergetic group shrank dramatically, and one tumor even disappeared (Figure 8A; dotted circle). The tumor weight declined significantly in the chemotherapy, PDT and synergetic therapy groups (Figure 8B, ANOVA, **P<0.01, ***P<0.001). Specifically, the average tumor weight was only 0.08 g in the synergetic group. Meanwhile, no obvious morphological changes were found in the heart, liver, spleen, lung or kidney from all groups following 12 days of treatment (Figure 8C). These results indicate that either chemotherapy or PDT alone can reduce the tumor volume. More importantly, compared to any single treatment, the synergy of chemotherapy and PDT from HCPT@NMOFs-RGD provides much better curative efficacy without obvious side effects. This may broaden the application of HCPT in chemotherapy and contribute to the comprehensive treatment of HCC.

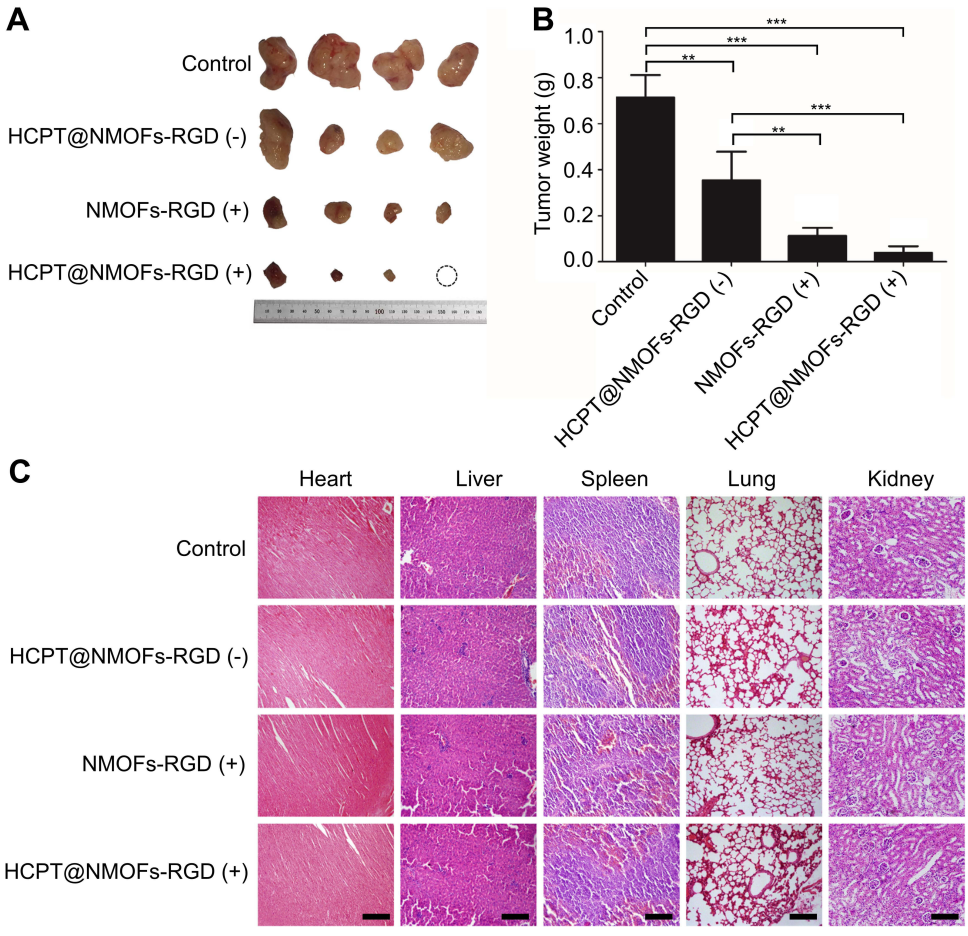

Figure 8 The reduction of tumors in HCC-bearing mice following chemo-, photodynamic-, and synergistic therapy. (**A**) Images of tumors following different treatments at 12 days post treatment (dpt). Note that one tumor in the HCPT@NMOFs-RGD (+) group completely disappeared. (**B**) Statistical analysis of tumor weight at 12 dpt (ANOVA; **P<0.01, ***P<0.001). (**C**) Images of HE staining of the heart, liver, spleen, lung and kidney. "(+)" and "(−)" represent samples with or without laser irradiation at 655 nm, respectively. Scale bar in (**C**): 50 μm.

Conclusion

In summary, the synthesized NMOFs-RGD emit bright fluorescence with low biotoxicity and excellent biocompatibility. The novel nanocomposites HCPT@NMOFs-RGD not only modify the hydrophobicity of HCPT but also accomplish tumor targeting via specific binding to integrin $\alpha_v\beta_3$-expressing cells. Furthermore, HCPT@NMOFs-RGD play a synergistic chemo- and photodynamic therapeutic role and show enhanced curative efficiency in HCC without significant side effects. HCPT@NMOFs-RGD offers an imaging-guided drug delivery and theranostic platform and may provide a promising approach for the treatment of HCC.

Acknowledgments

The authors thank Dr. Zhiyuan Gong (Molecular Biology Laboratory, Department of Biological Sciences, National University of Singapore, Singapore) for providing transgenic zebrafish *Tg* (*fabp10:rtTA2s-M2; TRE2:EGFP-kras*^{G12V}). This work was supported by the Chinese National Natural Science Foundation (81971739).

Disclosure

The authors report no conflicts of interest in this work.

References

1. Qiu Z, Li H, Zhang Z, et al. A pharmacogenomic landscape in human liver cancers. *Cancer Cell*. 2019;36(2):179–193.e111. doi:10.1016/j.ccell.2019.07.001
2. Wei L, Lee D, Law CT, et al. Genome-wide CRISPR/Cas9 library screening identified PHGDH as a critical driver for Sorafenib resistance in HCC. *Nat Commun*. 2019;10(1):4681. doi:10.1038/s41467-019-12606-7
3. Zhang PF, Wei CY, Huang XY, et al. Circular RNA circTRIM33-12 acts as the sponge of MicroRNA-191 to suppress hepatocellular carcinoma progression. *Mol Cancer*. 2019;18(1):105. doi:10.1186/s12943-019-1031-1
4. Cho Y, Kim JW, Kim JK, et al. Phase I radiation dose-escalation study to investigate the dose-limiting toxicity of concurrent intra-arterial chemotherapy for unresectable hepatocellular carcinoma. *Cancers*. 2020;12(6):1612. doi:10.3390/cancers12061612
5. Wang H, Liu Y, Xu M, Cheng J. Azido-galactose outperforms azido-mannose for metabolic labeling and targeting of hepatocellular carcinoma. *Biomater Sci*. 2019;7(10):4166–4173. doi:10.1039/c9bm00898e
6. Zu Y, Meng L, Zhao X, et al. Preparation of 10-hydroxycamptothecin-loaded glycyrrhizic acid-conjugated bovine serum albumin nanoparticles for hepatocellular carcinoma-targeted drug delivery. *Int J Nanomed*. 2013;8:1207–1222. doi:10.2147/IJN.S40493
7. Xu J, Wan Z, Tang M, et al. N^6-methyladenosine-modified CircRNA-SORE sustains sorafenib resistance in hepatocellular carcinoma by regulating β-catenin signaling. *Mol Cancer*. 2020;19(1):163. doi:10.1186/s12943-020-01281-8
8. Coussens NP, Braisted JC, Peryea T, Sittampalam GS, Simeonov A, Hall MD. Small-molecule screens: a gateway to cancer therapeutic agents with case studies of food and drug administration-approved drugs. *Pharmacol Rev*. 2017;69(4):479–496. doi:10.1124/pr.117.013755
9. Zhu X, Li J, Qiu X, Liu Y, Feng W, Li F. Upconversion nanocomposite for programming combination cancer therapy by precise control of microscopic temperature. *Nat Commun*. 2018;9(1):2176. doi:10.1038/s41467-018-04571-4
10. Yang R, Zhang Z, Fu S, et al. Charge and size dual switchable nanocage for novel triple-interlocked combination therapy pattern. *Adv Sci*. 2020;7(18):2000906. doi:10.1002/advs.202000906
11. Maslanka Figueroa S, Fleischmann D, Beck S, et al. Nanoparticles mimicking viral cell recognition strategies are superior transporters into mesangial cells. *Adv Sci*. 2020;7(11):1903204. doi:10.1002/advs.201903204
12. Sharma N, Kumari RM, Gupta N, Syed A, Bahkali AH, Nimesh S. Poly-(lactic-co-glycolic) acid nanoparticles for synergistic delivery of epirubicin and paclitaxel to human lung cancer cells. *Molecules*. 2020;25(18):4243. doi:10.3390/molecules25184243
13. Kumari M, Sharma N, Manchanda R, et al. PGMD/curcumin nanoparticles for the treatment of breast cancer. *Sci Rep*. 2021;11(1):3824. doi:10.1038/s41598-021-81701-x
14. Lee J, Kwak JH, Choe W. Evolution of form in metal-organic frameworks. *Nat Commun*. 2017;8:14070. doi:10.1038/ncomms14070
15. Van Vleet MJ, Weng T, Li X, Schmidt JR. In situ, time-resolved, and mechanistic studies of metal-organic framework nucleation and growth. *Chem Rev*. 2018;118(7):3681–3721. doi:10.1021/acs.chemrev.7b00582
16. Wang Y, Feng L, Zhang K, et al. Uncovering structural opportunities for Zirconium metal-organic frameworks via linker desymmetrization. *Adv Sci*. 2019;6(23):1901855. doi:10.1002/advs.201901855
17. Li H, Lv N, Li X, et al. Composite CD-MOF nanocrystals-containing microspheres for sustained drug delivery. *Nanoscale*. 2017;9(22):7454–7463. doi:10.1039/c6nr07593b
18. Hultgren NW, Fang JS, Ziegler ME, et al. Slug regulates the Dll4-Notch-VEGFR2 axis to control endothelial cell activation and angiogenesis. *Nat Commun*. 2020;11(1):5400. doi:10.1038/s41467-020-18633-z
19. Carneiro J, Gonçalves A, Zhou Z, Griffin KE, Kaufman NEM, Vicente M. Synthesis and in vitro PDT evaluation of new porphyrins containing meso-epoxymethylaryl cationic groups. *Lasers Surg Med*. 2018;50(5):566–575. doi:10.1002/lsm.22824
20. Zhu C, Kros JM, Cheng C, Mustafa D. The contribution of tumor-associated macrophages in glioma neo-angiogenesis and implications for anti-angiogenic strategies. *Neuro Oncol*. 2017;19(11):1435–1446. doi:10.1093/neuonc/nox081
21. Lu C, Han HD, Mangala LS, et al. Regulation of tumor angiogenesis by EZH2. *Cancer Cell*. 2010;18(2):185–197. doi:10.1016/j.ccr.2010.06.016
22. Viallard C, Larrivée B. Tumor angiogenesis and vascular normalization: alternative therapeutic targets. *Angiogenesis*. 2017;20(4):409–426. doi:10.1007/s10456-017-9562-9

23. Stubb A, Guzmán C, Närvä E, et al. Superresolution architecture of cornerstone focal adhesions in human pluripotent stem cells. *Nat Commun*. 2019;10(1):4756. doi:10.1038/s41467-019-12611-w
24. Ablooglu AJ, Kang J, Petrich BG, Ginsberg MH, Shattil SJ. Antithrombotic effects of targeting alphaIIbbeta3 signaling in platelets. *Blood*. 2009;113(15):3585–3592. doi:10.1182/blood-2008-09-180687
25. Westerfield M. *The Zebrafish Book: A Guide for the Laboratory Use of Zebrafish (Brachydanio Rerio)*. Eugene, OR: University of Oregon Press; 1993.
26. Bresolí-Obach R, Busto-Moner L, Muller C, Reina M, Nonell S. NanoDCFH-DA: a silica-based nanostructured fluorogenic probe for the detection of reactive oxygen species. *Photochem Photobiol*. 2018;94(6):1143–1150. doi:10.1111/php.13020
27. Chen Y, Liu W, Shang Y, et al. Folic acid-nanoscale gadolinium-porphyrin metal-organic frameworks: fluorescence and magnetic resonance dual-modality imaging and photodynamic therapy in hepatocellular carcinoma. *Int J Nanomed*. 2019;14:57–74. doi:10.2147/IJN.S177880
28. Avci ME, Keskus AG, Targen S, et al. Development of a novel zebrafish xenograft model in ache mutants using liver cancer cell lines. *Sci Rep*. 2018;8(1):1570. doi:10.1038/s41598-018-19817-w
29. Wang YJ, Liu W, Yuan B, et al. The application of methylprednisolone nanoscale zirconium-porphyrin metal-organic framework (MPS-NPMOF) in the treatment of photoreceptor degeneration. *Int J Nanomed*. 2019;14:9763–9776. doi:10.2147/IJN.S225992
30. Prochowicz D, Kornowicz A, Lewinski J. Interactions of native cyclodextrins with metal ions and inorganic nanoparticles: fertile landscape for chemistry and materials science. *Chem Rev*. 2017;117(22):13461–13501. doi:10.1021/acs.chemrev.7b00231
31. Tan LL, Li H, Zhou Y, et al. Zn^{2+}-triggered drug release from biocompatible zirconium MOFs equipped with supramolecular gates. *Small*. 2015;11(31):3807–3813. doi:10.1002/smll.201500155
32. Liu J, Yang Y, Zhu W, et al. Nanoscale metal-organic frameworks for combined photodynamic & radiation therapy in cancer treatment. *Biomaterials*. 2016;97:1–9. doi:10.1016/j.biomaterials.2016.04.034
33. Venkatachalapathy D, Shivamallu C, Prasad SK, et al. Assessment of chemopreventive potential of the plant extracts against liver cancer using HepG2 cell line. *Molecules*. 2021;26(15):4593. doi:10.3390/molecules26154593
34. Duan J, Yu Y, Li Y, Yu Y, Sun Z. Cardiovascular toxicity evaluation of silica nanoparticles in endothelial cells and zebrafish model. *Biomaterials*. 2013;34(23):5853–5862. doi:10.1016/j.biomaterials.2013.04.032
35. Sun Y, Zhang G, He Z, Wang Y, Cui J, Li Y. Effects of copper oxide nanoparticles on developing zebrafish embryos and larvae. *Int J Nanomed*. 2016;11:905–918. doi:10.2147/IJN.S100350
36. Cheng D, Shami GJ, Morsch M, Chung RS, Braet F. Ultrastructural mapping of the zebrafish gastrointestinal system as a basis for experimental drug studies. *Biomed Res Int*. 2016;2016:8758460. doi:10.1155/2016/8758460
37. Westphal RE, O'Malley DM. Fusion of locomotor maneuvers, and improving sensory capabilities, give rise to the flexible homing strikes of juvenile zebrafish. *Front Neural Circuits*. 2013;7:108. doi:10.3389/fncir.2013.00108
38. Rosenblum D, Joshi N, Tao W, Karp JM, Peer D. Progress and challenges towards targeted delivery of cancer therapeutics. *Nat Commun*. 2018;9(1):1410. doi:10.1038/s41467-018-03705-y
39. Peñate Medina T, Gerle M, Humbert J, et al. Lipid-iron nanoparticle with a cell stress release mechanism combined with a local alternating magnetic field enables site-activated drug release. *Cancers*. 2020;12(12):3767. doi:10.3390/cancers12123767
40. Florczak A, Deptuch T, Lewandowska A, et al. Functionalized silk spheres selectively and effectively deliver a cytotoxic drug to targeted cancer cells in vivo. *J Nanobiotechnology*. 2020;18(1):177. doi:10.1186/s12951-020-00734-y
41. Siegler EL, Kim YJ, Chen X, et al. Combination cancer therapy using chimeric antigen receptor-engineered natural killer cells as drug carriers. *Mol Ther*. 2017;25(12):2607–2619. doi:10.1016/j.ymthe.2017.08.010
42. Lakshmikanthan S, Sobczak M, Chun C, et al. Rap1 promotes VEGFR2 activation and angiogenesis by a mechanism involving integrin $\alpha v\beta_3$. *Blood*. 2011;118(7):2015–2026. doi:10.1182/blood-2011-04-349282
43. Jia Z, Song L, Zang F, et al. Active-target T_1-weighted MR imaging of tiny hepatic tumor via RGD modified ultra-small Fe_3O_4 nanoprobes. *Theranostics*. 2016;6(11):1780–1791. doi:10.7150/thno.14280
44. Song Z, Chang Y, Xie H, Yu X-F, Chu PK, Chen T. Decorated ultrathin bismuth selenide nanosheets as targeted theranostic agents for in vivo imaging guided cancer radiation therapy. *NPG Asia Mater*. 2017;9(10):e439. doi:10.1038/am.2017.167
45. Nguyen AT, Emelyanov A, Koh CH, et al. A high level of liver-specific expression of oncogenic Kras(V12) drives robust liver tumorigenesis in transgenic zebrafish. *Dis Model Mech*. 2011;4(6):801–813. doi:10.1242/dmm.007831
46. Sueangoen N, Tantiwetrueangdet A, Panvichian R. HCC-derived EGFR mutants are functioning, EGF-dependent, and erlotinib-resistant. *Cell Biosci*. 2020;10:41. doi:10.1186/s13578-020-00407-1
47. Rao TC, Ma VP, Blanchard A, et al. EGFR activation attenuates the mechanical threshold for integrin tension and focal adhesion formation. *J Cell Sci*. 2020;133(13):jcs238840. doi:10.1242/jcs.238840
48. D'Amora M, Raffa V, De Angelis F, Tantussi F. Toxicological profile of plasmonic nanoparticles in zebrafish model. *Int J Mol Sci*. 2021;22(12):6372. doi:10.3390/ijms22126372
49. Cai X, Xie Z, Ding B, et al. Monodispersed copper(I)-based nano metal-organic framework as a biodegradable drug carrier with enhanced photodynamic therapy efficacy. *Adv Sci*. 2019;6(15):1900848. doi:10.1002/advs.201900848
50. Muhanna N, Jin CS, Huynh E, et al. Phototheranostic porphyrin nanoparticles enable visualization and targeted treatment of head and neck cancer in clinically relevant models. *Theranostics*. 2015;5(12):1428–1443. doi:10.7150/thno.13451
51. Celli JP, Spring BQ, Rizvi I, et al. Imaging and photodynamic therapy: mechanisms, monitoring, and optimization. *Chem Rev*. 2010;110(5):2795–2838. doi:10.1021/cr900300p
52. Zou Y, Long S, Xiong T, et al. Single-molecule Förster resonance energy transfer-based photosensitizer for synergistic photodynamic/photothermal therapy. *ACS Cent Sci*. 2021;7(2):327–334. doi:10.1021/acscentsci.0c01551
53. Liu G, Zeng Y, Lv T, et al. High-throughput preparation of radioprotective polymers via Hantzsch's reaction for in vivo X-ray damage determination. *Nat Commun*. 2020;11(1):6214. doi:10.1038/s41467-020-20027-0